Effect of Powder Recycling in Electron Beam Melting on the Surface Chemistry of Alloy 718 Powder

Effect of Powder Recycling in Electron Beam Melting on the Surface Chemistry of Alloy 718 Powder

HANS GRUBER, MIKAEL HENRIKSSON, EDUARD HRYHA, and LARS NYBORG

Process-induced degradation of the powder feedstock in additive manufacturing may have a negative influence on the final properties of built components. Consequently, it may lower the cost-effectiveness of powder bed additive manufacturing, which relies on recycling of the nonconsumed powder. This is especially the case for production of high-performance aero engine components where high material and process reliability is required. This study comprises a detailed investigation on the degradation of Alloy 718 powder during multicycle electron beam melting (EBM). The surface-sensitive analysis methods, X-ray photoelectron spectroscopy (XPS) and Auger electron spectroscopy (AES), were combined with scanning electron microscopy (SEM) to depict the differences in surface morphology, and surface composition of powder samples exposed to varying numbers of re-use cycles. The results show a significant change in surface characteristics after exposing the powder to the process and the environment in the build chamber. The virgin powder is covered mainly by a relatively thin and homogeneous oxide layer. The re-used powder, however, has undergone transformation to a heterogeneous oxide layer, rich in thermodynamically stable Al-rich oxide particulates, which started already during the first build cycle. Significant growth of the Al-rich oxide occurs *via* selective oxidation of Al under the conditions in the build chamber, including both pick-up of oxygen from the process atmosphere and redistribution of initial surface-bound oxygen from less-stable products like Ni-oxide and/or hydroxide.

https://doi.org/10.1007/s11661-019-05333-7

I. INTRODUCTION

ALLOY 718 (also known as Inconel® 718 or IN718) is a well-known age-hardenable Ni-Fe-base superalloy. Owing to its high Nb content, Alloy 718 is primarily strengthened by the disk-shaped gamma double prime phase (Ni_3Nb) which maximizes its strength at temperatures up to around 650 °C. As Alloy 718 also contains Al and Ti, the cuboidal or spherically shaped, matrix-coherent gamma prime ($Ni_3(Al, Ti)$) also contributes to the precipitation strengthening. Alloy 718 exhibits excellent mechanical properties, corrosion resistance and oxidation resistance, at a wide range of temperatures. Besides being extensively used for gas turbine disks and compressor blades in aircraft engines, it finds service in a wide range of industrial application areas such as rocket motors, nuclear reactors, as well as in the oil industry.[1–3]

To date, Alloy 718 is predominately produced using the ingot-metallurgy route, including double melting (VIM + VAR/ESR) or triple melting (VIM + VAR + ESR) followed by homogenization, forging, and finally machining: a sequence associated with high cost and long lead times.[4] Even though Alloy 718 is considered to have a relatively good fabricability, its high strength, poor thermal conductivity, and work-hardening characteristics make both forging and machining challenging steps in the production chain. In addition, high material costs and increasing demands on sustainable production routes further incentivize minimal machining and improved buy-to-fly ratio.[1,5]

The foregoing aspects motivate the recent rising interest that electron beam melting (EBM), a member of the powder bed fusion additive manufacturing (AM) family, has seen from both industry, and research community. Being able to produce complex-shaped metal components without tooling and extensive machining, while also reducing the total lead time, EBM has been recognized as a potential candidate for the aerospace industry as a means of obtaining high-performance, light-weight components through structural optimization.[6] However, to fully utilize the potential that AM offers, high reliability, and robustness is required from both material and process. In

HANS GRUBER, MIKAEL HENRIKSSON, EDUARD HRYHA, and LARS NYBORG are with the Department of Industrial and Materials Science, Chalmers University of Technology, Gothenburg, Rännv. 2A, 412 96 Gothenburg, Sweden. Contact e-mail: hans.gruber@chalmers.se
Manuscript submitted February 17, 2019.
Article published online July 2, 2019

particular, the amount of material imperfections must be held at a minimum to meet the requirements for fatigue and fracture mechanical properties, especially under the hostile conditions at which aerospace engine components operate.

Even though additive manufacturing has been subjected to extensive research during the recent years, there is still lack of knowledge in many different aspects. One such area is the effect of the powder feedstock material on the process stability, and/or quality of the produced components. While several powder characteristics have been suggested as being critical for maintaining a reliable process, too few direct correlations have been established to express which of these characteristics are significant or not.[7,8] Furthermore, a possible degradation of the excess, nonconsumed powder that has been exposed to the process environment in the build chamber has initiated another branch within the additive manufacturing research area, namely powder recycling. Considering that the nonconsumed powder has to be re-used to reach high material efficiency, any possible powder degradation issues induced by multicycle re-use have to be thoroughly addressed.

As in traditional powder metallurgy, the high specific surface area of the AM powder feedstock makes it susceptible to surface reactions such as oxidation. Even though EBM is marketed as a process with high reliability on the material properties, the high temperatures at which the powder bed is held during the process may have an effect on the powder surface chemistry, with subsequent formation of damage-relevant oxide inclusions and bonding defects in the built components.[9,10] A number of studies have been performed to assess the recyclability of Alloy 718 powder, mainly in laser beam processes. In this case, only minor changes in both physical and chemical powder properties are generally reported. An increasing oxygen content in the AM fabricated material has, however, been identified as a limiting factor for the permitted number of re-use cycles, due to the resulting reduction in component ductility.[11] For Ti-6Al-4V, which is the most widely studied material for EBM, it has been shown that the bulk oxygen level of powder as well as EBM fabricated material increases progressively along with powder recycling.[12–14] The main source of oxygen has in this case been described as adsorption of water on the powder surface during powder handling, grit blasting, and sieving, followed by a pick-up of oxygen during high-temperature exposure in the build chamber.[12,13] Also in the case of EBM processing of Alloy 718, increasing oxygen levels have been reported in both powder and solid samples after a few build cycles.[12] In line with these findings, indications of both powder surface oxidation during powder recycling and a corresponding increase in oxide-rich defects in the built components, have been observed.[3] However, no systematic and detailed studies regarding the mechanisms behind surface oxidation of Alloy 718 powder during progressive EBM processing have been published yet, which is therefore the objective of this study.

II. MATERIALS AND METHODS

This study comprises a detailed comparison between virgin and re-used Alloy 718 powder for EBM. The term re-used (or recycled) refers to the nonconsumed powder that has been exposed to the process for varying numbers of machine cycles. The material under observation was commercial prealloyed powder with a chemical composition conforming with the specification of Alloy 718, presented in Table I. The concentrations of oxygen and nitrogen in the powder, as measured by combustion analysis, were both in the order of 150 ppm (see Table III). The powder was produced by plasma atomization of a wire precursor material in an argon atmosphere, as described in Reference 15, and had a particle size distribution of 45 to 105 μm. The powder was provided by Arcam EBM, Sweden.

The re-used powder samples were collected from an Arcam A2X EBM system, with a 4.2 melting theme version, located at University West, Trollhättan, Sweden. All powder samples were collected from the process chamber after operating the machine at standard melt strategies and process parameters, provided by the machine supplier. To work efficiently, the electron beam requires a partial vacuum. Therefore, before the electron beam was started, the pressure inside the process chamber was lowered to around 10^{-8} bar. During beam operation, a small quantity of grade 5 purity helium (< 2 ppm O_2) was injected, which raised the pressure in the build chamber to around 10^{-6} bar.[16] From this, an oxygen partial pressure of around 4×10^{-9} bar inside the build chamber has been estimated. For Alloy 718, a powder bed temperature of 975 °C ± 25 °C has been noted as optimal to reach a stable process.[17] This temperature is maintained in the powder bed throughout the whole build process. Furthermore, as a slight bonding between the metal particles is required to avoid repulsion of the powder from the negative charge induced by the electron beam, every powder layer was preheated by the electron beam, resulting in powder sintering before the actual melting.[18,19] After the process, the nonconsumed powder above the start plate was in the form of a "cake" of sintered powder, surrounding the built components, as indicated in the schematic overview of the EBM machine interior illustrated in Figure 1. The position of powder sampling has been indicated in this figure as well.

In total, this study comprises 14 build cycles, spanning over a total build time of around 500 hours (not including time for heat-up and cool-down), and initially involved 80 kg of virgin Alloy 718 powder that was loaded into the EBM machine before the start of cycle 1. After each build cycle, small samples of loose powder (below 10 g), scraped from the outer wall in the lower end of the sintered cake (see Figure 1), were collected for microscopy and chemical analyses.

Between each machine cycle, the excess powder in the sintered cake was recovered following a procedure specified by the machine producer. This involves grit blasting to separate individual metal particles that are sintered together in the powder cake, mixing with the nonconsumed powder from the powder hoppers and

Table I. Chemical Composition of the Alloy 718 Powder as Provided by the Powder Producer

Element	Ni	Co	Cr	Mo	Ti	Mn	Nb	B	P	Ta	Al	Fe	Si	S	C
Wt Pct	54.1	0.04	19.0	2.99	1.02	0.12	4.97	0.001	0.004	< 0.01	0.52	17.12	0.06	< 0.001	0.03
At. Pct	53.38	0.04	21.16	1.80	1.23	0.13	3.10	0.01	0.01	< 0.01	1.12	17.75	0.12	< 0.001	0.14

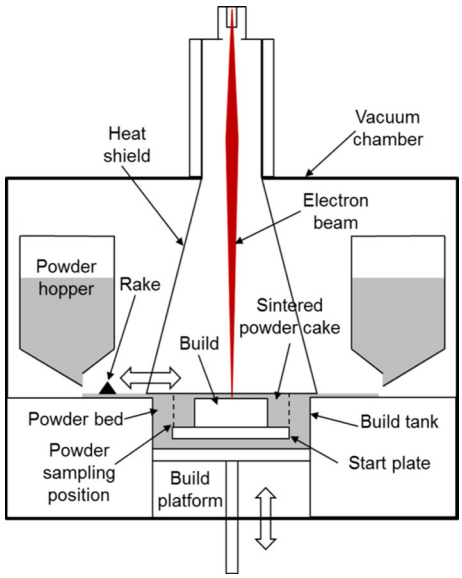

Fig. 1—Schematic illustration of the EBM machine interior. Position of powder sampling has been indicated.

finally sieving to remove any powder agglomerates. For practical reasons, an addition of 20 pct virgin powder was required to reach the build height of cycle 6. No further addition of fresh powder was done during this study.

The surface morphology of the as-received and the re-used powder samples was characterized using a Leo Gemini high-resolution scanning electron microscope (SEM, LEO GmbH, Oberkochen, Germany) equipped with a secondary electron in-lens detector, which allows for enhanced phase contrast and lateral resolution compared to a conventional secondary electron detector. A solid-state energy dispersive X-ray spectrometer (EDS) from Oxford Instruments (X-Max, Oxford Instruments Ltd., High Wycombe, UK) connected to the SEM was used for qualitative analysis of the phases present on the powder surface and on the powder cross sections. Samples for surface characterization were prepared by slightly pressing the metal powder into aluminum plates that could be mounted onto an SEM sample holder. Samples for powder cross section analysis were prepared from a mixture of powder and conductive bakelite resin that was mounted using Struers standard metallography recipe. Thereafter, the cross sections were obtained either by mechanical grinding and polishing or by ion polishing using a Leica TIC3X broad ion beam instrument (BIB).

An overall chemical analysis of the powder surface was performed by means of X-ray photoelectron spectroscopy (XPS) using a PHI 5500 instrument equipped with a monochromatic aluminum Kα source (1486.6 eV). The powder samples were prepared by distributing a thin layer of powder on a carbon tape. The photoelectrons originate from an area of around 0.8 mm in diameter (~ 100 particles), which means that the signal represents the overall chemistry of the analyzed powder surfaces. Survey spectra were recorded for identification of chemical elements present on the powder surfaces. Narrow scan energy regions corresponding to the elements of interest were selected for detailed analysis followed by curve fitting to obtain the chemical composition of the surface and the chemical state of the elements. Surface compound thickness and chemical composition depth profiling from the as-received surface down to an etch depth of 500 nm were obtained by altering XPS analysis and argon ion etching using an accelerating voltage of 4 kV and a beam raster size over an area of 2.5×2.5 mm^2. This gave an etch rate of 7.8 nm min^{-1} as calibrated on Ta_2O_5.

The SEM/EDS and XPS were complemented with local chemical analysis by means of Auger electron spectroscopy (AES) using a PHI 700 AES from Physical Electronics. Compared with SEM/EDS, AES offers the possibility to perform laterally resolved surface chemical analysis with an interaction depth of less than 10 nm below the sample surface. The electron accelerating voltage was 10 kV and the beam current was 10 nA, enabling a nominal analytical lateral resolution of 10 to 20 nm. Image registration was done within intervals of maximum two minutes to ensure that the data were acquired at the intended location. Argon ion etching capabilities of the system allowed for composition depth profiling. Etch rates of 0.66 nm min^{-1} were obtained by using an ion gun acceleration voltage of 1 kV and a beam raster size of 3×3 mm^2. The etch rate was calibrated on a standard Ta_2O_5 sample and hence is referring to Ta_2O_5 units.

Oxygen measurements of the powder samples were performed by means of inert gas fusion (combustion analysis) on a LECO ON836 elemental analyzer to quantify the extent of oxidation during powder re-use. Similarly, the nitrogen level was measured to detect any possible reactions with nitrogen during the process. Oxygen and nitrogen measurements were done at Höganäs AB, and were performed in accordance with the standards SS-EN 10276-2 and SS-EN ISO 15351, respectively. For each sample set, at least three individual samples were evaluated.

III. RESULTS

A. *SEM/EDS Analysis*

Qualitative analysis on a large number of metal particles in the virgin and re-used state was accomplished by means of SEM and EDS analysis. Representative surface morphologies of the virgin powder are presented in Figures 2(a) through (c). Generally, the virgin powder exhibits a surface that is visually free from secondary phases and contamination species. As already described in Reference 3, nonmetallic inclusions with a size of a few μm were occasionally observed on the powder surface and inside the powder. In most cases, their blocky shape and yellow tinge in the optical microscope identified them as Ti-rich nitride particles. This was confirmed from EDS analysis which gave rise to significantly intense peaks from Ti and N, corresponding to a concentration of close to 50 at. pct each for both elements. Similarly, others were identified as Al-rich oxide inclusions.[3] Figures 2(d) through (l) show typical surface morphologies of powder after varying number of re-use cycles, as observed at different magnifications in the SEM. In Figures 2(d) through (f), a sample collected after the first 70 hours of processing shows that already after the first build cycle, a significant amount of nanosized particulates has

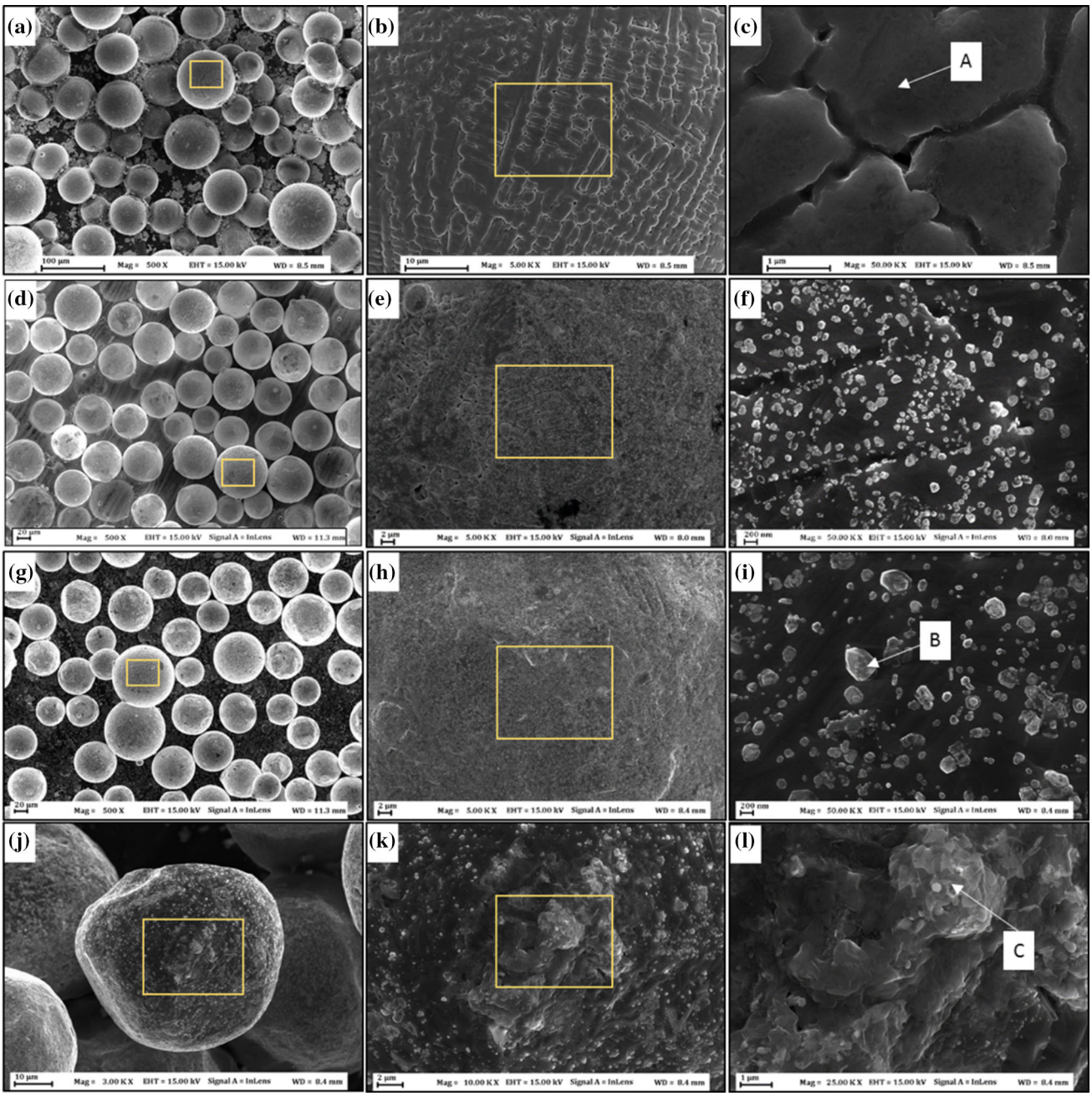

Fig. 2—Secondary electron images of the Alloy 718 powder surface morphology (*a*) to (*c*) virgin powder; (*d*) to (*f*) from bottom of build after 1 cycle; (*g*) to (*l*) from bottom of build after 14 cycles; corresponding EDS analysis data are presented in Table II.

formed on the powder surface. Powder from the following build cycles [up to cycle number 14, see Figures 2(g) to (i)] indicates that the average number and size of these features tend to increase with increasing number of re-use cycles. Furthermore, on occasion, the recycled powder surface also exhibits areas covered with thick and porous products, as shown in Figures 2(j) through (l). In reference to the matrix, EDS point analysis spectra obtained from a large number of these features exhibit intense peaks of Al and O, which indicates that it consists of Al-rich oxide. Compositional information on the observed features obtained from EDS point analysis are listed in Table II. Regarding the data in Table II, however, it should be noted that the interaction volume from where the EDS signal is generated is generally much larger than the size of the particulates features, which means that a significant contribution of the signal originates from the surrounding matrix material. It should also be pointed out that the accuracy of EDS is generally limited when it comes to detection of light elements. Therefore, the figures in Table II should mainly be considered as a preliminary qualitative assessment of the powder surface chemistry, preceding the much more accurate analysis by XPS and AES, presented in Sections III–B and III–C below.

On the cross section of the powder after 14 re-use cycles, see Figure 3, it can be seen that the Al-rich oxide particulates are present only within a region very close to the original surface. Usually, their size is in the range of 50 to 200 nm.

The oxygen levels in the virgin and the re-used powders as measured by inert gas fusion (combustion analysis) are presented in Table III. In addition to the build cycle number, the total (accumulated) process time of all preceding cycles has been included as additional information. However, it should be noted that both build cycle number and process time serve only as rough indicators of the powder condition.

Nevertheless, as seen in Table III, the increasing amount of oxide during powder re-use is confirmed by a continuously increasing oxygen level in the powder samples collected throughout the powder recycling study. The nitrogen level on the other hand is relatively stable at around 150 ppm in all powder samples irrespective to the condition of the powder.

B. *XPS Analysis*

Figure 4 shows the XPS survey spectra measured on powder in virgin state and after 14 re-use cycles. The spectra shown are recorded after slight ion etching, corresponding to around 1 nm from the as-received surface, to remove surface absorbed species. As indicated in the figure, photoelectron peaks corresponding to nickel and the major alloying elements (Ni2p, Cr2p, Fe3p, Nb3d, Ti2p, Al2p, Mo3d) together with carbon (C1s), nitrogen (N1s), and a strong oxygen (O1s) signal were registered for both powder conditions. The nitrogen peak corresponds to the presence of TiN, as also seen in SEM. As previously reported,[20,21] segregation

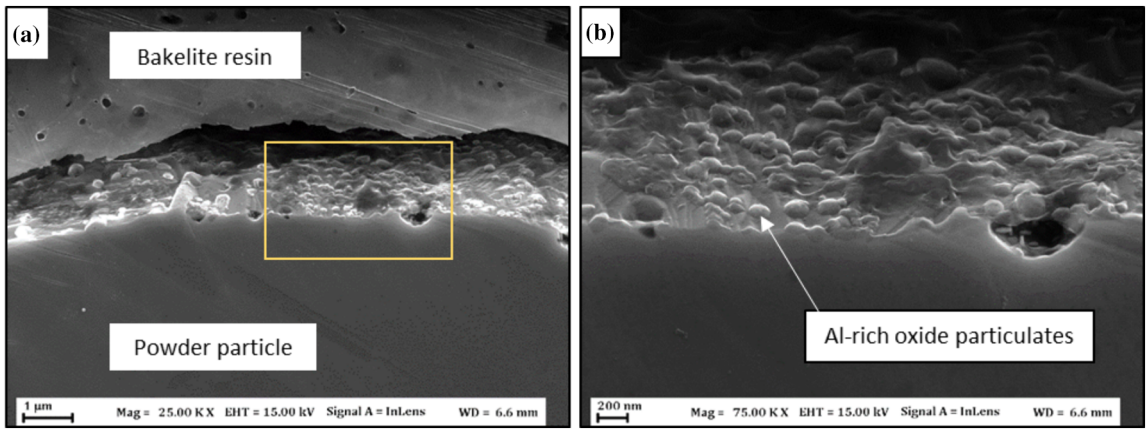

Fig. 3—Broad ion beam cross section of a powder sample collected after build cycle number 14. (*a*) Field of view; (*b*) Al-rich oxide particulates at higher magnification.

Table II. EDS Point Analysis Data from Areas in Fig. 3

		Chemical Composition (At Pct)									
Location	Structure	Ni	Cr	Fe	Nb	Mo	Ti	Al	O	Ca	S
A	matrix	52.3	21.7	19.8	2.4	1.5	1.3	1.1	—	—	—
B	Al-rich oxide particulate	24.2	11.4	10.1	1.5	0.8	1.2	18.9	31.9	—	—
C	Al-rich oxide cluster	5.6	2.3	1.9	3.0	—	5.9	28.3	40.1	10.3	2.6

of sulfur to the metal–gas interface during high-temperature exposure explains the sulfur peak (S2p) in the spectrum obtained from the as-received surface of the re-used powder.

Figure 5 illustrates the elemental concentration depth profiles for virgin and recycled powder, respectively, as measured by XPS analysis. For improved visualization, data recorded in the region closest to the as-received surface are presented separately in Figures 5(b) and (d).

As shown in Figure 4, it is evident that the surface of both kinds of powder have similar chemistry. However, a significant difference in element distribution through the etch depth is observed. Both powder conditions have a high oxygen content at the as-received surface, decreasing directly after initial etching, which implies that they are both covered by a thin oxide layer. The major differences between the two powder conditions arise as a consequence of the much thicker oxide particulates on the re-used powder, in agreement with the observations by SEM. This is shown by the oxygen level in the recycled powder which is considerably higher down to larger etch depths compared to that of the virgin powder. Also, enrichment of Al on the surface of the recycled powder is more pronounced as compared to the virgin powder, which further indicates the selective oxidation of Al on the powder surface. Mainly, the strong carbon signal on the original surface corresponds to adsorbed hydrocarbons and is removed already after slight ion etching. The remaining carbon signal after ion etching most likely originates from presence of MC carbides, which is known to form directly from the melt during solidification,[4,22] but is not considered further in this study.

Curve fitting of the XPS peaks from the high-resolution narrow scans for oxygen and most of the oxide-forming elements was performed to determine the chemical state evolution along the depth from the as-received surface. As seen in Figures 6(a) and (b), there is a clear difference between the peaks for Al in the virgin and re-used powder. For the virgin powder, the Al peak is positioned at binding energy levels which could be an indication of Al in a spinel type oxide such as $NiAl_2O_4$, as reported in Reference 23. In the case of the recycled powder, the Al peak in Figure 6(b) is closer to values for Al_2O_3 positions reported in many references.[23] Also, due to a stronger oxidation of Al to the surface of the recycled powder, the Al oxide peak is more pronounced compared to the virgin powder, both at the as-received surface and after ion etching. A clear difference is also seen in the oxygen peaks after initial ion etching, Figures 6(c) and (d). A considerable portion of the oxygen signal of the virgin powder originates from the transition metal oxides at around 530 eV (Cr_2O_3, NiO, Fe_2O_3, TiO_2, Nb_2O_5), while the recycled powder shows a strong shift towards 532 eV binding energy, corresponding to Al_2O_3. As noted above, this signal is present to much larger etch depths in the recycled powder compared to the virgin powder, indicating that the thickness of the oxidized region/features is much greater in the recycled powder, and that it is not connected to any transition metal hydroxide, which would have been removed after initial ion etching. Hence, the detection of Al oxide to greater etch depth in combination with the O^{2-} peak indicative for Al_2O_3 for the O1s-region suggest that the oxide appearing in particulate form on the surface of re-used powder is Al-rich oxide, possibly Al_2O_3. As indicated in Figures 6(e) and (f), Ni hydroxide is possibly present on the outermost surface of both virgin and re-used powder. The presence of a weak Ni metal peak in the signal from the as-received surface and its instant rise in intensity after initial ion etching indicate that Ni mainly exists in hydroxide/oxide state in a region close to the as-received surface. Furthermore, this thin layer may also be related to presence of spinel oxide $NiAl_2O_4$ whose peaks for both Ni2p and O1s cannot be easily distinguished from those of Ni hydroxide; both the spinel and $Ni(OH)_2$ have similar characteristic peak positions at around 856.2 eV.[23] For both kinds of powder, basically all other metallic elements are mainly present in oxide state in a region close to the as-received surface. Analysis of the oxygen peak indicates decreasing contributions from both transition metal oxide (Ni, Fe, Cr, Ti, Nb-base) at around 530 eV and Al_2O_3 oxide at approximately 532 eV with increasing etch depths. The changes in relative amounts of oxide and metal states for other oxide-forming elements as well as the shift from oxide (or hydroxide) reflect the similar distribution in depth for their surface oxide products (Figures 6(a) to (j)). In the case of Ti as shown in Figures 6(i) and (j), the position of the peaks obtained close to the original surface indicates the presence of a mixed type of oxide and/or the presence of several different Ti-oxides. In accordance with the above SEM observations, besides Ti-oxide, peaks in Figures 6(i) and (j) correspond also to TiN and possibly some Ti-metal after extended ion etching. Since the Ti-oxide is mainly removed already after 3 to 5 nm, it can be assumed the TiN is the main Ti-compound present with greater thickness on the surface.

Curve fitting of the presented peaks above provides further indications on the difference in oxidation between the two powder conditions. Figures 7(a) and (b) show the concentrations of elements in oxide or hydroxide state (cation concentration) along the first 100 nm from the original surface of the virgin and recycled powder, respectively. The insets show the elements constituting the oxide/hydroxide closest to the as-received surface. The steep decrease in cation concentration of all elements except that of Al shows that they are present as oxide/hydroxide state in a very thin region close to the surface of both kinds of powder, rather than in thicker reaction products as in the case of Al, for which the decay in cation content is much lower with increasing etch depth. As expected, the largest difference between the two powder conditions lies in the Al cation concentration due to the large amount of Al-rich oxide particulates observed on the surface of the re-used powder. Consequently, the amount of Al in oxide state is considerably larger in the re-used powder down to an etch depth of around 100 nm, where it stabilizes at a level which is similar for both powder conditions.

Table III. Oxygen Levels in Virgin and Re-used Powder Samples Measured by Inert Gas Fusion

Powder Sample	Accumulated Process Time (h)	Average Oxygen Level (ppm)	Individual Oxygen Measurements (ppm)
Virgin	—	146	131, 148, 159
Re-used, After Cycle #1	70	215	209, 215, 221
Re-used, After Cycle #14	500	266	257, 264, 277

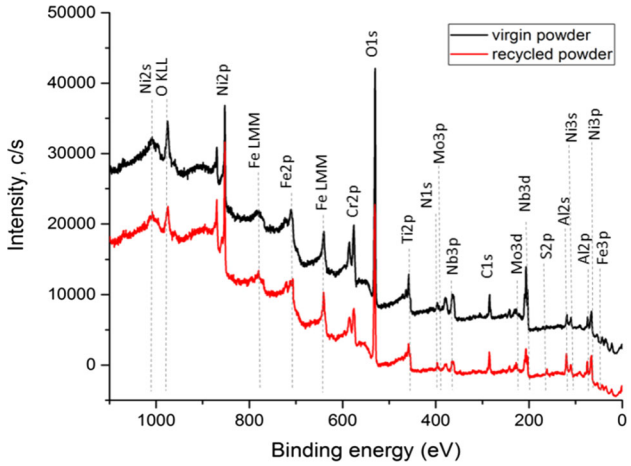

Fig. 4—XPS survey spectra from virgin and re-used powder at a depth of around 1 nm from the as-received surface.

C. *AES Analysis*

Areas of variations in the surface oxide layer morphology of the virgin powder surface, as shown in Figures 8(a) and (b), were analyzed by AES depth profiling, see Figure 9. In agreement with the overall chemical analyses by XPS (Figure 7), the high O-level reflects the oxide character of the surface and hence, alloying elements on the as-received surface can be depicted as being present in their oxide state. Furthermore, as seen in the XPS results, the high surface content of Al is shown in both spectra. Hence, Figure 9(a) shows that the outermost region of the visually homogeneous areas in Figure 8(a) (point A) consist of a Ni-Al-rich oxide, together with Cr, Ti, and Fe oxide mainly present a small depth below the original surface. The relatively high Ni/Al atomic ratio in the outermost surface suggests that this part of the surface mainly consist of Ni-based hydroxide/oxide, but still with potential presence of Al in oxidized state. As shown in Figure 9(b), the flake-like areas in Figure 8(b) (point B) has a higher aluminum content and a Ni/Al atomic ratio that is closer to that of $NiAl_2O_4$. Together these two compounds coincide with the overall XPS composition profile shown in Figure 7(a), for which Al in oxide state is present as a major element across the whole surface layer, together with Ni in oxide state closest to the as-received surface. Furthermore, it shows that the difference in surface oxide visible in SEM relates to the extent of aluminum oxide on the powder surface. Based on the oxygen depth profiles in Figures 9(a) and (b), the Ni-rich oxide layer is estimated to have a thickness of around 2 nm in Ta_2O_5 units.

The AES analysis of the powder after 14 re-use cycles is shown in Figure 10. Significant peaks from Al and O in the spectra obtained from the bright particulate features (point 1, Figure 10(a)) confirms high concentrations of Al-rich oxide phase. Compared to the AES analysis of the virgin powder in Figure 9, there is a low Al concentration in the spectrum obtained from the as-received surface in between the oxide particulates of the recycled powder (point 6, Figure 10(a)). This suggests that growth of the oxide particulates has resulted in a depletion of Al in adjacent areas.

Instead, a transition metal oxide/hydroxide layer is found in these regions, as compared to the previously observed Ni and Al-rich oxide/hydroxide layer as seen on the virgin powder. The fact that the recycled powder is partly covered by a thin transition oxide layer is also expected from Figure 6(d) since the oxygen signal at 530 eV is reduced after initial ion sputtering.

IV. DISCUSSION

Summarizing the above results, the main differences in surface chemical characteristics between the virgin and re-used powder are schematically illustrated in Figure 11. The virgin powder is mainly covered by a relatively thin and homogeneous Ni-base, Al-containing oxide/hydroxide layer. The surface of the re-used powder, however, contains a considerable amount of Al-rich oxide particulates that grow as a consequence of exposing the powder to the conditions in the EBM process chamber. Since growth of the particulates partly occurs *via* redistribution of aluminum and oxygen from the homogeneous oxide layer, a thin transition metal oxide/hydroxide layer is formed in between the oxide particulates, most likely during the subsequent exposure to air at lower temperatures, including the handling. Similar for both powder conditions is the presence of Ni-containing hydroxide/oxide in the outermost surface region. In the case of the virgin powder, this signal may originate from a thin Ni-hydroxide and/or from Ni-Al spinel oxide, that is possibly present in areas with higher aluminum level, which cover parts of the surface (Figure 8(b)).

In the case of the re-used powder, however, it is shown that the areas in between the oxide particulates contain a transition metal oxide, depleted in Al. In this case, Ni is most likely present in the form of Ni hydroxide. The Al-rich oxide on the virgin powder has most likely formed at higher temperatures during powder fabrication. The Ni-hydroxide/oxide layer on

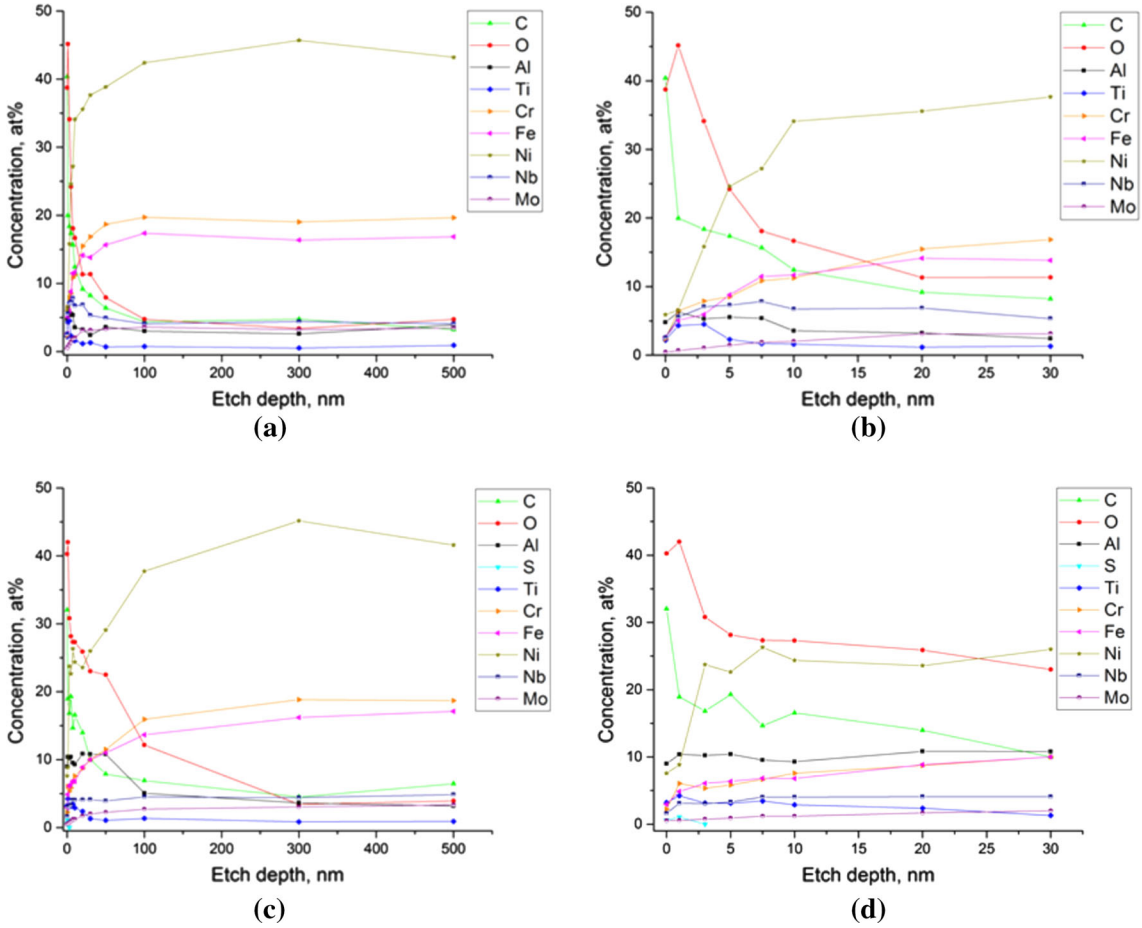

Fig. 5—XPS depth profile of chemical elements in the region close to the initial powder surface for (*a*) and (*b*) virgin and (*c*) and (*d*) re-used powder after 14 cycles.

the other hand has most likely formed at lower temperatures during cooling or as a result of exposing the powder to the ambient air.[24,25]

Figure 12 presents the temperature dependence of the equilibrium oxygen partial pressure for the metal/metal oxide systems that have been encountered in the above analyses. For each of the curves in the figure, conditions above the curve are oxidizing, and conditions below are reducing, indicating oxide decomposition. Even though the data in Figure 12 are based on oxidation of pure metals, it is still relevant for assessing the relative stability of oxides in an alloying system. The dotted lines in the figure indicate the approximate condition for the position of sampling in the EBM process chamber—a temperature of around 1000 °C at a theoretical oxygen partial pressure of around 4×10^{-9} bar. However, besides from residual air at the vacuum conditions in the chamber, the presence of moisture and less-stable oxygen-containing phases, such as hydroxide and base metal oxides (NiO, Cr_2O_3, and Fe_2O_3), on the powder surface, serve as an additional source of oxygen when released during heating and melting of the powder. Consequently, the actual oxygen partial pressure in the vicinity of the powder surface is higher than the theoretical and can possibly rise to values in the order of 10^{-7} bar.[26] Many of the alloying elements have much lower equilibrium oxygen partial pressure which means that thermodynamically, the oxygen partial pressure has to be kept at much lower values to avoid formation of oxides on the powder surface. For this reason, presence of several oxides can be expected at such conditions.[27]

Furthermore, decomposition of the less-stable bulk metal oxides (as indicated in Figure 11) enables an additional source of oxygen.[28] At lower temperatures, when exposing the powder to air or moisture during powder recovery/handling, additional oxygen pick-up takes place in form of bulk metal oxides, hydroxides, and/or from adsorption of water molecules. Upon heating in the next build cycle, redistribution of oxygen from these less-stable compounds into more stable particulate oxides, such as Al_2O_3, takes place at the high operation temperature. Since the stable oxides will persist also at very high temperatures and/or low oxygen partial pressures, as the oxygen level increases over the re-use cycles, the total amount of stable oxides such as Al_2O_3 will increase.

As observed in earlier studies,[3,26,29] during the actual melting process, there is a risk of transferring of nonmetallic phases (mainly Al-rich oxide and TiN) from the powder to the components. Furthermore, since

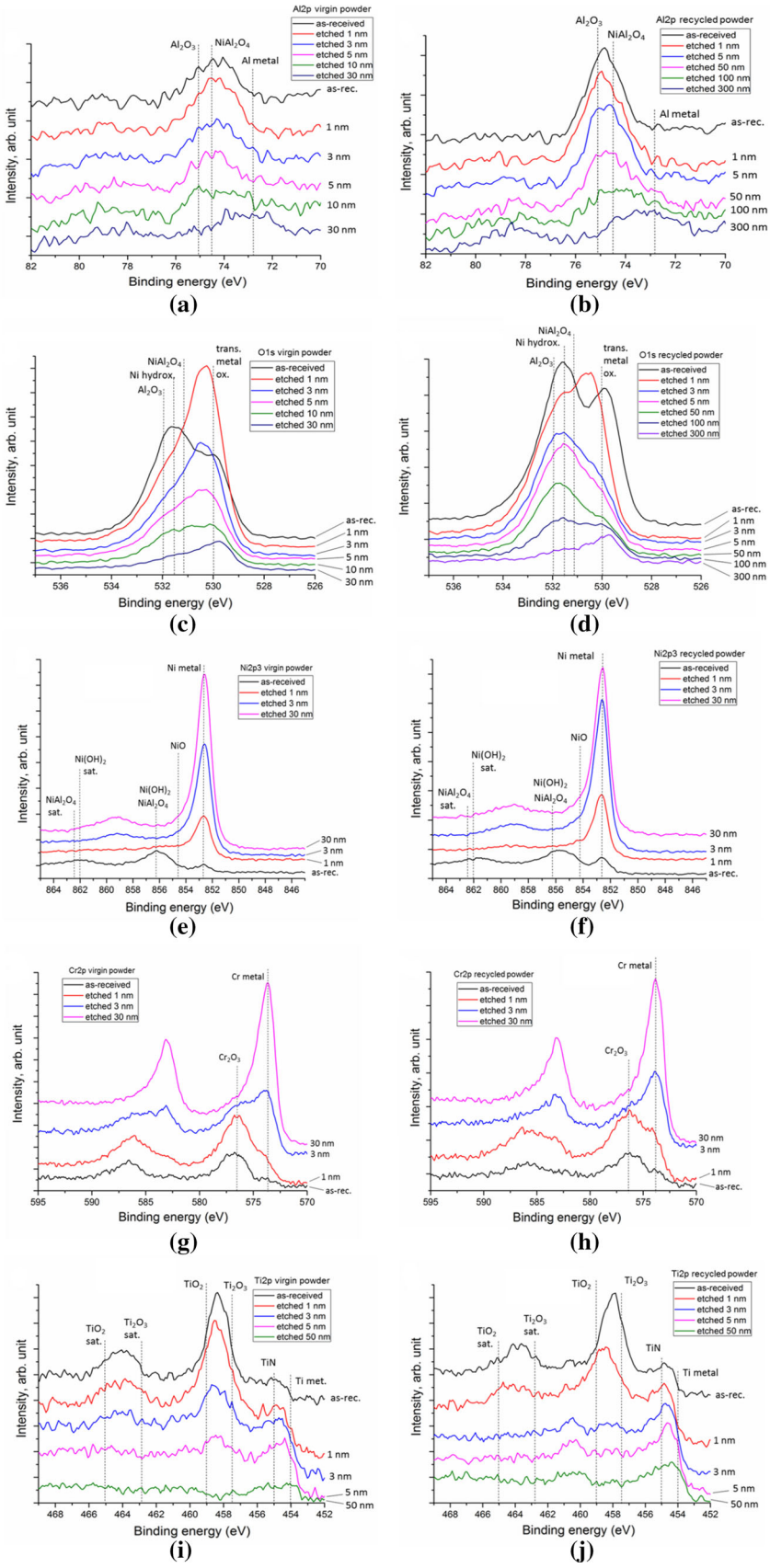

Fig. 6—XPS detailed scans recorded from virgin and re-used 14 times powder at different depths from the as-received surface; (*a*) and (*b*) Al2p; (*c*) and (*d*) O1s; (*e*) and (*f*) Ni2p; (*g*) and (*h*) Cr2p; (*i*) and (*j*) Ti2p.

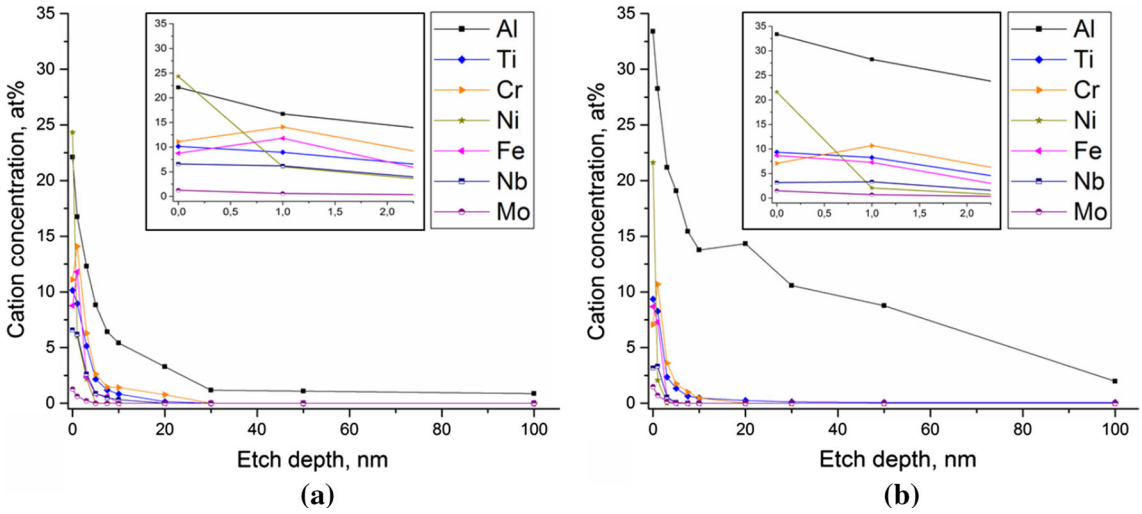

Fig. 7—Cation concentration along etch depth in (*a*) virgin and (*b*) 14 times re-used powder.

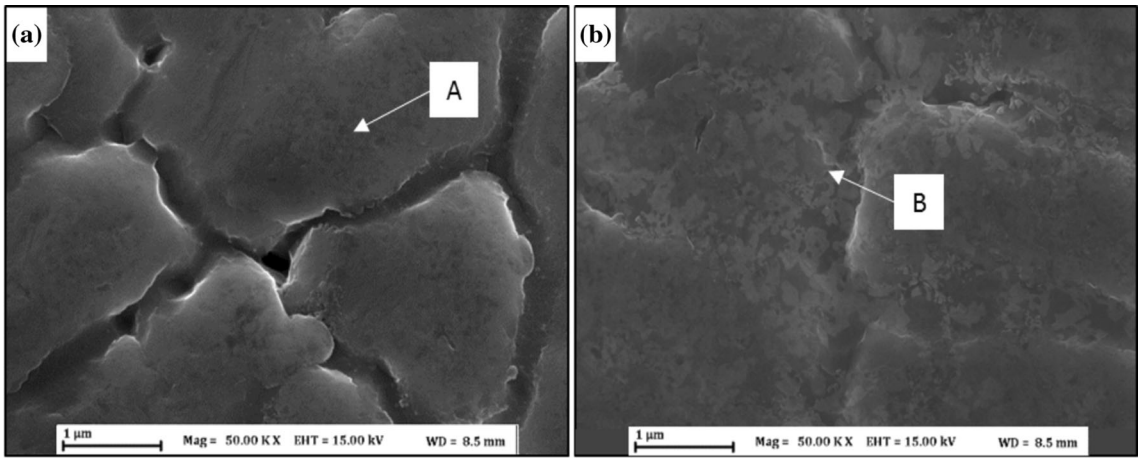

Fig. 8—Variations in the surface oxide layer morphology of the virgin powder; (*a*) visually homogeneous areas; (*b*) flake-like areas observed in SEM.

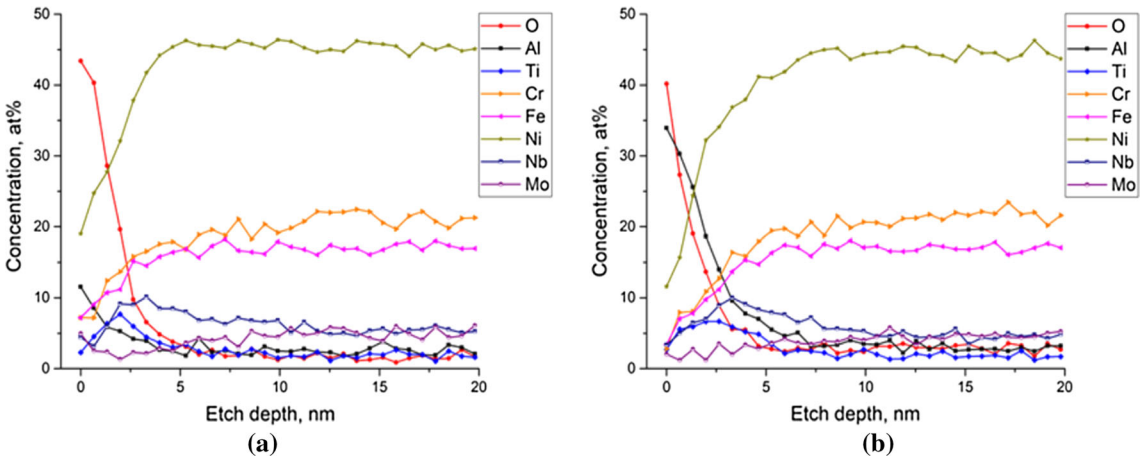

Fig. 9—AES depth profiles from virgin Alloy 718 powder shown in Fig. 8. Representative point analyses from (*a*) visually homogeneous areas; (*b*) flake-like areas observed in SEM.

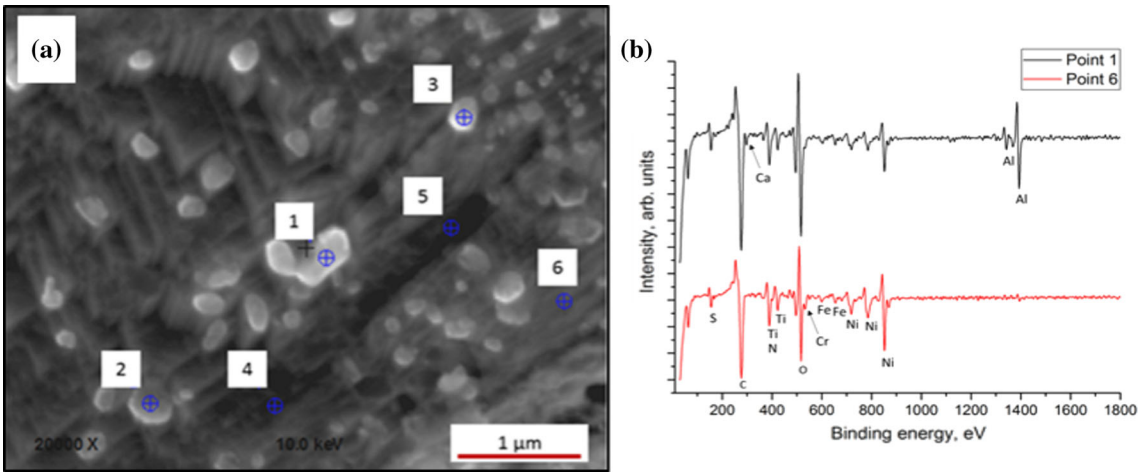

Fig. 10—AES analysis of a powder sample after 14 re-use cycles; (*a*) field of view; (*b*) spectra obtained from an Al-rich oxide particulate and the surrounding matrix material in the as-received surface.

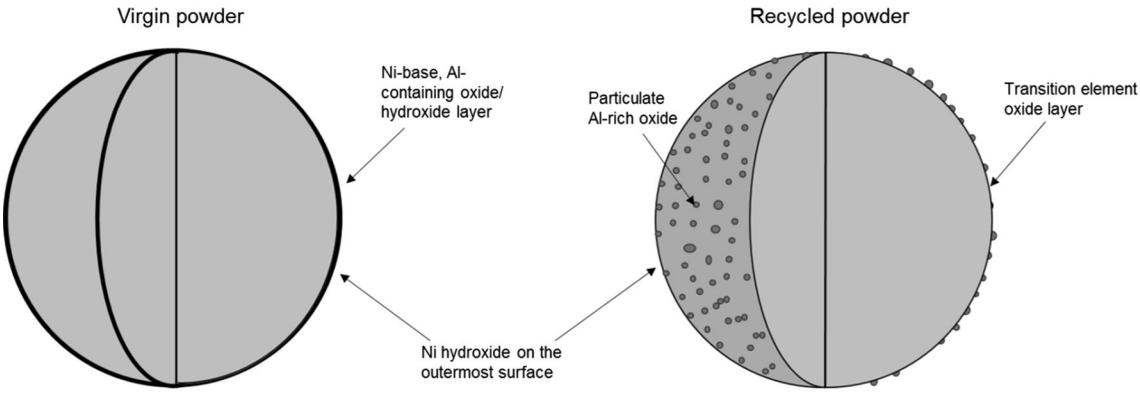

Fig. 11—Schematic illustration of the main differences in surface morphologies between the virgin and re-used powder. Oxygen redistribution from a relatively homogeneous oxide layer to form the thicker particulate oxide phase is illustrated by a thinner oxide/hydroxide film on the re-used powder as compared to the virgin powder.

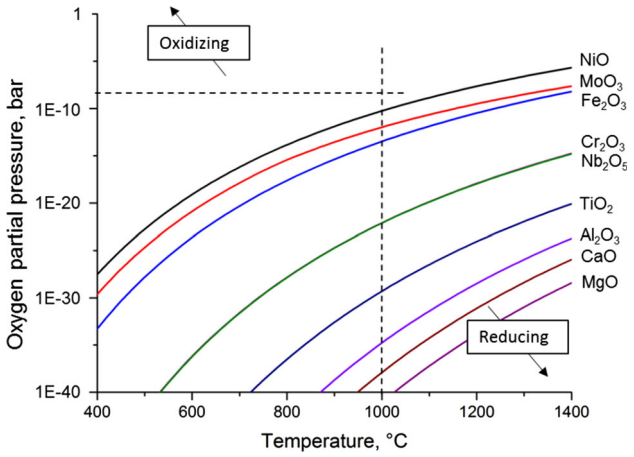

Fig. 12—Metal/metal oxide equilibria diagram. Plotted using data from the software HSC Chemistry version 8.0. Note the overlap of Cr_2O_3 and Nb_2O_5.

these phases tend to accumulate into larger sized clusters or oxide flakes, they act as potential damage initiation sites, especially under cyclic loading conditions.[26,30]

It should be noted that the total amount of oxide phase in the powder supply can be significantly reduced by regular addition of fresh powder in between the build cycles. Even so, there is a great benefit in reducing the amount of nonmetallic phases in the powder to ensure an acceptable cleanliness also for applications with a low permissible level of inclusion contamination. Furthermore, the portion of Al tied up in oxide state has also been made unavailable for its initial purpose as precipitation strengthening element through formation of the gamma prime phase, $Ni_3(Al, Ti)$, which further underlines the benefit in limiting the oxide formation in EBM-processed Alloy 718.

As seen in Figure 12, high temperature together with low oxygen partial pressure (vacuum annealing) decreases oxide stability and may lower the amount of oxide that can form on the powder surfaces. However, the high stability of Al_2O_3 would require very high temperatures and/or low oxygen concentrations, which tend to complicate the process, especially during production on an industrial scale. Exposing the re-used powder to reducing atmospheres is another means of reducing stable oxides at temperatures lower than those

required for vacuum annealing.[31] Another suggestion is improvement of the oxygen level in the EBM chamber, as it is done during vacuum sintering of such metal powder through repeated flushing of the vacuum chamber with inert gas.[31] Similarly, controlled powder handling and/or possibly by degassing the powder before the process can lower the amount of adsorbed moisture and hydroxide available for oxide formation.

Even though the tendency of Al to form Al_2O_3 is very high, its low concentration in Alloy 718 sets a mass barrier for the amount that can be transported towards the surface through solid state diffusion.[2] As described in Reference 31, temperatures around 1000 °C are extremely dangerous from the perspective of powder oxidation due to the high diffusion rates in the solid for the alloying elements and at the same time unfavorable thermodynamic conditions in terms of oxide dissociation. Hence, decreasing the temperature to lower diffusivity of, *e.g.,* Al is desirable from this point of view. However, in the present EBM machine configuration this is not a feasible option since the process stability is dependent on maintaining the process around 1000 °C. For instance, an increased tendency for powder smoking and spatter from the melt pool has been observed at temperatures below 950 °C.[17]

V. CONCLUSIONS

Virgin and re-used Alloy 718 EBM powder were studied to investigate process-induced surface chemistry alterations during multicycle EBM processing. The findings can be summarized as follows:

1. The virgin Alloy 718 plasma-atomized powder surface is covered by a relatively thin and homogeneous oxide layer, formed by a mixed Al- and transition metal hydroxide/oxide layer.
2. Selective oxidation of Al while exposing the powder to the EBM process and the environment in the build chamber results in a transformation from the thin, initial layer to a coarse, heterogeneous oxide layer characterized by thermodynamically stable Al-rich oxide particulates.
3. A significant amount of nanosized Al-rich oxide particulates form on the powder surface already after the first build cycle and tend to grow in number and size with the increasing number of re-use cycles. The increasing amount of oxide is confirmed by the increasing oxygen level with progressive re-use.
4. Growth of the oxide particulates occurs due to pick-up of oxygen from the process atmosphere and from redistribution of oxygen from thermodynamically less-stable oxide and hydroxide compounds on the powder surface.

ACKNOWLEDGMENTS

The work was performed in the framework of the Centre for Additive Manufacturing – Metal (CAM^2), supported by Vinnova. The authors would also like to acknowledge the financial support from SIP LIGHTer and AoA Production at Chalmers. The authors also express appreciation to Jonas Olsson at Production Technology Center, Trollhättan, Sweden for providing the samples and to Höganäs AB for chemical bulk analysis of the powder samples.

REFERENCES

1. Maher, *Alloy 718 Data Sheet Quick Facts Alloy 718 Data Sheet Industry Specifications Melting Practices Machinability*, pp. 1–5.
2. C.T. Sims, N.S. Stoloff, and W.C. Hagel: *Superalloys 2*, 2nd ed., Wiley, New York, 1987.
3. H. Gruber, P. Karimi, E. Hryha, and L. Nyborg: *Powder Metall. Prog.*, 2018, vol. 18 (1), pp. 40–48.
4. J.E. Matz and T.W. Eagar: *Metall. Mater. Trans. A*, 2002, vol. 33 (8), pp. 2559–67.
5. D. Zhu, X. Zhang, and H. Ding: *Int. J. Mach. Tools Manuf.*, 2013, vol. 64, pp. 60–77.
6. S. Liu, Q. Li, J. Liu, W. Chen, and Y. Zhang: *Engineering*, 2018, vol. 4 (2), pp. 277–85.
7. A. Leicht, R. Shvab, E. Hryha, and L. Nyborg, *Paper in Proceedings, SPS16*, Lund, Sweden, 2016.
8. X. Wang, X. Gong, and K. Chou: *Proc. Inst. Mech. Eng.*, 2017, vol. 231 (11), pp. 1890–1903.
9. D. Bourell, J.P. Kruth, M. Leu, G. Levy, D. Rosen, A.M. Beese, and A. Clare: *CIRP Ann.*, 2017, vol. 66 (2), pp. 659–81.
10. S. Das: *Adv. Eng. Mater.*, 2003, vol. 5 (10), pp. 701–11.
11. M. Renderos, A. Torregaray, M.E. Gutierrez-Orrantia A. Lamikiz, N. Saintier, and F. Girot: *Mater. Charact.*, 2017, vol. 134, pp. 103–13.
12. H.P. Tang, M. Qian, N. Liu, X.Z. Zhang, G.Y. Yang, and J. Wang: *Jom*, 2015, vol. 67 (3), pp. 555–63.
13. P. Nandwana, W.H. Peter, R.R. Dehoff, L.E. Lowe, M.M. Kirka, F. Medina, and S.S. Babu: *Metall. Mater. Trans. B*, 2016, vol. 47 (1), pp. 754–62.
14. V. Petrovic and R. Niñerola: *Aircr. Eng. Aerosp. Technol.*, 2015, vol. 87 (2), pp. 147–55.
15. M.I. Moulding and J. Kroeger: *Powder Inject. Mould. Int.*, 2011, vol. 5 (4), pp. 55–57.
16. Online document: Arcam AB, Welcome to Manufacturing Unbound. http://www.arcam.com/wp-content/uploads/arcamebm-corp-brochure-fnlv3.pdf Accessed 08 May 2019.
17. W.J. Sames, Texas A&M University, 2015.

18. E. Chauvet, P. Kontis, E.A. Jägle, B. Gault, D. Raabe, C. Tassin, J. Blandin, R. Dendievel, B. Vayre, S. Abed, and G. Martin: *Acta Mater.*, 2017, vol. 142 (17), pp. 82–94.
19. D. Deng, Linköping University, 2018.
20. R. Hales, A.C. Hill, and R.K. Wild: *Corros. Sci.*, 1973, vol. 13 (5), pp. 325–36.
21. H. Herman: *Treatise on Materials Science & Technology*, 2nd ed., Elsevier, Amsterdam, 1973.
22. A.M. Ritter and M.F. Henry: *J. Mater. Sci.*, 1982, vol. 17, pp. 73–80.
23. A. Velon and I. Olefjord: *Oxid. Met.*, 2001, vol. 56 (5), pp. 425–52.
24. L. Nyborg and I. Olefjord: *Powder Metall. Int.*, 1988, vol. 20 (2), pp. 11–16.
25. I. Olefjord and L. Nyborg: *Powder Metall.*, 1985, vol. 28 (4), pp. 237–43.
26. H.E. Helmer, Friedrich-Alexander-Universität Erlangen Nürnberg, 2016.
27. Y.N. Zhang, X. Cao, P. Wanjara, and M. Medraj: *Acta Mater.*, 2013, vol. 61 (17), pp. 6562–76.
28. C. Gierl-Mayer, R. Calderon, and H. Danninger: *Jom*, 2016, vol. 68 (3), pp. 920–27.
29. H. Gruber, C. Luchian, E. Hryha, and L. Nyborg, Chalmers University of Technology, unpublished research, 2018.
30. D. Krewerth, T. Lippmann, A. Weidner, and H. Biermann: *Int. J. Fatigue*, 2016, vol. 84, pp. 40–52.
31. E. Hryha, E. Dudrova, and L. Nyborg: *J. Mater. Process. Technol.*, 2012, vol. 212 (4), pp. 977–87.